Article:

Mella, D., Brevis, W. and Susmel, L. orcid.org/0000-0001-7753-9176 (2020) Spanwise wake development of a bottom-fixed cylinder subjected to vortex-induced vibrations. Ocean Engineering, 218. 108280. ISSN 0029-8018

https://doi.org/10.1016/j.oceaneng.2020.108280

Highlights

Spanwise wake development of a bottom-fixed cylinder subjected to vortex-induced vibrations

Daniel Mella,Wernher Brevis,Luca Susmel

- Proper Orthogonal Decomposition can extract main coherent cylinder motions
- Coherent motion of the maximum cylinder response is an elliptical-type trajectory
- Wake and motion spanwise synchronisation maximised at the highest cylinder response
- Bottom-up desynchronisation develops after the maximum cylinder response is achieved
- 2S and 2P vortex modes observed along the cylinder span and across flow rates

Spanwise wake development of a bottom-fixed cylinder subjected to vortex-induced vibrations

Daniel Mella[a,*], Wernher Brevis[b] and Luca Susmel[a]

[a]*Department of Civil and Structural Engineering, The University of Sheffield, Sheffield, UK*

[b]*Department of Hydraulics and Environmental Engineering and Department of Mining Engineering, Pontifical Catholic University of Chile, Santiago, Chile*

ARTICLE INFO

Keywords:
Fluid-structure interaction (FSI)
Vortex shedding
Proper orthogonal decomposition (POD)
Bottom-fixed cylinder
Synchronisation
Vortex pattern

ABSTRACT

This study analyses the spanwise wake dynamics and structural response of a bottom-fixed cylinder subjected to a range of open-channel fully developed turbulent flows. The experiments were performed with a Reynolds number ranging between 4.5×10^2 and 1×10^3. The cylinder free end response and the flow velocity in the wake were measured using Particle Image Velocimetry and image-based tracking techniques. The cylinder had a significant modulated response, from which a Proper Orthogonal Decomposition revealed a clockwise elliptical-type trajectory at the maximum cylinder response. Wake dynamic analysis showed that the maximum response is achieved when the cylinder motion and vortex shedding frequencies are equal (i.e. synchronised) to the natural frequency of the structure measured in still water, and when this equivalence is preserved along the span of the cylinder. As the flow velocity increases, a spanwise bottom-up desynchronisation process develops moving towards the water surface. This process decreases the vortex-formation region strength along the span of the cylinder, reducing the maximum structural response and eventually changing the vortex shedding pattern. Despite the highly three-dimensional experimental conditions under significant turbulent incoming flows, the findings of previous studies based on simpler experimental models can still be used to broadly explain the observed desynchronisation process.

1. Introduction

Vortex induced vibrations (VIV) is a non-linear, self-governed, multi-degree-of-freedom (DOF) phenomenon that occurs due to the interaction between the vortex formation behind a body and its structural response (Williamson and Govardhan (2004)). VIV can be an important contributor to fatigue damage on numerous engineering problems, such as marine risers, large chimneys, heat exchanger tubes, to name a few. Thus, this phenomena has been the subject of constant research in the last decades (see, for example, the extensive reviews of Gabbai and Benaroya (2005); Williamson and Govardhan (2004); Sarpkaya (2004)). An important part of experimental VIV research involves the study of simplified cylindrical models. These experiments usually consist on rigid cylinders forced or free to vibrate in their crossflow direction and subjected to a range of uniform and low-turbulence flows. These simplified models have provided substantial insights into the nature of VIV. Khalak and Williamson (1996, 1997) showed that the mass ratio m^* (ratio between the oscillating structure and displaced fluid mass) has an impact on the range of reduced velocities U_r in which the cylinder response and the vortex shedding frequency are equal, called synchronisation region. Here, $U_\mathrm{r} = U_\mathrm{inlet}/(f_\mathrm{water} D)$, where U_inlet is the mean incoming flow velocity, f_water is the natural frequency of the structure measured in still water, and D is the diameter of the cylinder. Cylinders with low m^* develop three distinctive regimes within the synchronisation range: the initial branch, the upper branch, where the maximum response is achieved, and the lower branch. Govardhan and Williamson (2000) related each branch to different vortex shedding patterns using flow visualisation techniques. Williamson and Roshko (1988) used forced-vibration experiments to map these vortical structures as a function of the maximum cylinder displacement and U_r. The researchers observed three vortex patterns or modes: 2S mode (two single vortices per cycle) measured in the initial branch, 2P (two pairs of vortices at every oscillation) observed in the upper and lower branch, and a wake pattern presented only in forced vibration studies, called P+S (single and a pair of vortices per cycle of body motion). Later, Morse and Williamson (2009) found a new vortex mode in the upper branch which they called 2Po. In this mode, a weaker vortex in each pair per cycle was observed.

Different researchers have been trying to determine the applicability of simplified models to cases of increasing complexity, which are closer to engineering applications. Morse and Williamson (2009) satisfactorily predicted the maximum response and wake mode of a free-vibration cylinder using their vortex mode map. Nevertheless, they noted a random component on the cylinder response that could not be reproduced in its forced-vibration counterpart. The effect of the Reynolds number on VIV has been found to be more significant than previously thought. High Reynolds number experiments are characterised by a broader synchronisation range and higher maximum cylinder response (Raghavan and Bernitsas (2011); Wanderley and Soares (2015)). Jauvtis and Williamson (2004) analysed the effects of allowing an additional DOF (crossflow and streamwise response) on

*Corresponding author. D.A. Mella. Department of Civil and Structural Engineering, The University of Sheffield, Mappin Street, S1 3JD, Sheffield, UK. Telephone: 0114 222 5713 E-mail address: mvamellavivanco1@sheffield.ac.uk (Daniel Mella)

ORCID(s): 0000-0003-0642-1300 (D. Mella)

an elastically mounted rigid cylinder in terms of peak amplitudes, response branches, and vortex shedding modes. They found a new branch (called super-upper branch) for cylinders with $m^* < 6$. Within this branch, peak crossflow amplitudes reached up to $1.5D$, and a new vortex mode called 2T was observed. This new vortex pattern consists on a triplet of vortices each half-cycle of body motion. Additionally, the tested cylinder traced eight-type trajectories throughout its synchronisation range. Other studies observed different motion patterns, such as elliptical-type (Oviedo-Tolentino et al. (2014)), eight-type, or a combination of both (Kang and Jia (2013)). Kheirkhah et al. (2012, 2016) showed that the trajectory type depends on the structural coupling between the streamwise and crossflow motion. The spanwise variability of tapered, pinned and cantilever cylinders haven been used to study complex fluid-structure interactions. Labbé and Wilson (2007) simulated a three-dimensional cylinder and showed the importance of the spanwise length to capture the main features of the flow. Franzini et al. (2014) simultaneously tested a two-DOF cantilever cylinder, and a one-DOF elastically mounted rigid cylinder. Both cylinders had similar mass ratios, diameters, lengths, and damping values. The cantilever cylinder had a broader synchronisation region and a higher maximum crossflow amplitude of $1.15D$ compared to $0.9D$ of the rigid cylinder. Flemming and Williamson (2005) studied the response of a free-vibration, two-DOF pinned cylinder. For small streamwise amplitudes, the response agreed qualitatively well with the one-DOF cylinder of Govardhan and Williamson (2000). However, at large streamwise motions, peak crossflow amplitudes of approximately $1.5D$ and a new vortex mode called 2C, composed of two co-rotating vortices per half-cycle, were observed in the upper branch. In addition, Flemming and Williamson (2005) observed the simultaneous existence of two vortex patterns along the span of the cylinder. Hybrid modes were also found by Techet et al. (1998) on tapered cylinders. Voorhees et al. (2008) studied flow three-dimensionality on a one-DOF free-vibration cylinder. Flow visualisation at different heights along the span of the cylinder showed significant differences with the predictions obtained using the vortex modes map of Morse and Williamson (2009).

The multi-DOF, variable-amplitude, free-vibration experimental work on VIV has shown substantial differences with the simplified cylindrical models. The two-DOF variable-amplitude bottom-fixed cylinder subjected to VIV provides a compelling case to study how changes in the wake dynamics along the span of the cylinder affect its structural response, a condition commonly found in numerous engineering problems. Previous studies on bottom-fixed cylinders observed and characterised a motion history with a highly dominant coherent response around its maximum displacement and measured the vortex shedding frequency at discrete horizontal planes along the span of the cylinder (see, for example, Franzini et al. (2014); Oviedo-Tolentino et al. (2014)). The identification and characterisation of these coherent responses when the cylinder motion is highly modulated and the variability between the structural response and vortex shedding synchronisation along the span of the cylinder has not been fully addressed. For this, flow measurements were performed using a two-dimensional Particle Image Velocimetry (PIV) system at one vertical plane along the span of the cylinder and four horizontal planes at different water depths. This high-resolution system allowed to measure the wake dynamics and spanwise vortex shedding as the cylinder is subjected to a range of turbulent flows. Each PIV measurement was synchronised with a camera that recorded the free end displacement of the cylinder. The recordings were analysed with image-based tracking techniques to determine the spatiotemporal displacement of the cylinder.

This paper is organised as follows: a summary of the snapshot POD method is presented in Section 2. Experimental setup of a bottom-fixed cylinder subjected to a range of turbulent flows is given in Section 3. The results are separated into two Subsections: Subsection 4.1 is focused on the characterisation of the cylinder in terms of maximum amplitude, main frequency of oscillation, and coherent trajectory identification using POD. Subsection 4.2 presents the wake dynamics and spanwise vortex shedding variability along the span of the cylinder at different flow velocities. Conclusions are given in Section 5.

2. Proper Orthogonal Decomposition

The Proper Orthogonal Decomposition is a statistical technique based on the decomposition of spatiotemporal data into a linear combination of spatial basis functions or modes ($\mathbf{\Phi}$) and their time-dependent modal coefficients (α). POD provides a mathematical definition of energy-relevant structures, arranged in descending order, and a method for their extraction (Brevis and García-Villalba (2011)). As it will be shown later, the cylinder exhibits a single-frequency linear-elastic response along its span due mainly to its low deformation across U_r. Thus, the POD technique is suitable to extract the main coherent trajectories associated with the most dominant frequencies when the cylinder response is highly modulated. A review of this technique can be found in Berkooz et al. (1993); Chatterjee (2000). Here, the snapshot POD method is briefly described in the context of the cylinder motion history. Detailed information about this technique can be found in Sirovich (1987).

The spatiotemporal position of the cylinder is expressed in vector form as $\boldsymbol{x}_c(t_d) = (x(t_d), y(t_d))$, where $t_d = [1, 2, ..., N]$ and N is the number of data points. Likewise, the fluctuating part of the cylinder response $\boldsymbol{x}_c{}'$ is obtained after removing its temporal average $\overline{(\cdot)}$ position, $\boldsymbol{x}_c{}' = (x', y')$, where $x'(t_d) = x(t_d) - \overline{x}$ and $y'(t_d) = y(t_d) - \overline{y}$. The fluctuating part $\boldsymbol{x}_c{}'$ is separated in k vectors of equal size L ($KL = N$) and arranged in matrix form as

$$\boldsymbol{X} = \begin{bmatrix} x_1' & x_2' & \dots & x_K' \\ y_1' & y_2' & \dots & y_K' \end{bmatrix} \tag{1}$$

The dimensions of the assembled matrix are $2L\mathrm{x}K$. Each column in Eq. 1 is considered a snapshot and represents the

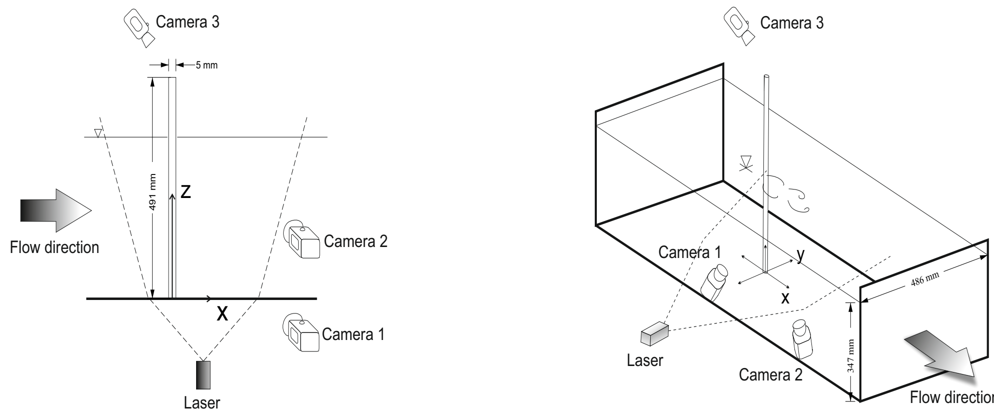

(a) PIV vertical plane. (b) PIV horizontal plane.

Figure 1: Experimental setup of a bottom-fixed cylinder subjected to a range of turbulent flows. Cylinder oscillations in transverse (y-axis) and longitudinal (x-axis) directions. The z-axis lies along the span of the cylinder. a) Vertical PIV plane. b) Horizontal PIV plane.

trajectory traced by the cylinder over L data points. Thus, the goal of using POD is to find the underlying coherent motion across all snapshots. Given a number of spatial modes $\boldsymbol{\Phi}_n$ and their corresponding modal coefficient α_n, the POD method finds the best fit for $\boldsymbol{X}$ in a least-square sense

$$\overline{\left\| \boldsymbol{X} - \sum_{n=1}^{K} \alpha_n \boldsymbol{\Phi}_n \right\|} \tag{2}$$

where $\|\cdot\|$ is the L_2-norm, and $n = [1, 2, ..., K]$. The POD method solves Eq. 2 through the solution of the following Eigenvalue problem

$$\boldsymbol{C}\boldsymbol{\Phi}_n = \lambda_n \boldsymbol{\Phi}_n \tag{3}$$

where $\boldsymbol{C} = \overline{\boldsymbol{X}^T \boldsymbol{X}}$ is the autocovariance matrix, and λ_n are the eigenvalues. The POD modes are orthonormal to each other and the eigenvalues represent the contribution of mode n to the total variance. The POD modes are usually arranged in descending order based on their corresponding λ_n to identify dominant patterns in the data. The relative of the i-th POD modal value is defined as

$$\epsilon_i = \frac{\lambda_i}{\sum_{n=1}^{K} \lambda_n} \tag{4}$$

3. Experimental Setup

The experiments were performed at the Civil and Structural Engineering water laboratory, University of Sheffield, United Kingdom. The flume was covered with clear cast acrylic sheets, leaving a squared cross-sectional area with width 486 mm and a longitudinal fixed slope of 0.001 m/m. A water depth of $H_w = 347$ mm was fixed using a computer-controlled system and a control gate located at the end of the flume. The Reynolds number R_e ranged between 4.5×10^2 and 1×10^3, which corresponds to the maximum flow rate of the facility. Here, $R_e = U_{inlet} D / \nu$, where U_{inlet} is the mean incoming flow velocity, D is the diameter of the cylinder, and ν is the kinematic viscosity of water. The incoming turbulent intensity was measured at 5% for all tested flow velocities. A 5 mm diameter hole with 10 mm depth was drilled on a squared acrylic base with width 165 mm. A cylinder made of clear cast acrylic (elastic modulus of 3.2×10^4 Kg cm^{-2}) was inserted into the hole and chemically welded fabricating a fixed end. The model was placed 10.5 m downstream, ensuring that the centre of the cylinder coincided with the middle of the flume's width. The cylinder configuration allowed the opposite end to vibrate in both the in-line (x-axis) and transverse (y-axis) flow directions. The z-axis lies along the span of the cylinder. The cylinder had a diameter of 5 mm, length of 491 mm, and m^* of 1.41. Figure 1 shows a sketch of the experimental setup.

The measurements were taken using a three-camera PIV system, consisting of a double-pulsed 532 nm wavelength Nd:YAG compact Laser of 200 mJ maximum power output, three MX 4M cameras of 2048x2048 pixel resolution, and a Programmable Time Unit (PTU) used to synchronise the cameras and laser trigger times. Higham and Brevis (2018) used the same water channel and PIV equipment to measure the wake around multiple obstacles. The water was seeded with Polyamide 12 of 100 µm mean particle size and 1.06 g cm^{-3} density. Two cameras recorded the spatio-temporal motion of these particles. Simultaneously, a third camera recorded the free end response of the cylinder. After adjusting the cameras and laser position, a calibration plate LaVision model 309-15 was placed on the desired measurement plane, and an image was taken. The markers within the calibration plate were used to correct the measurements for optical distortions and to establish a correspondence be-

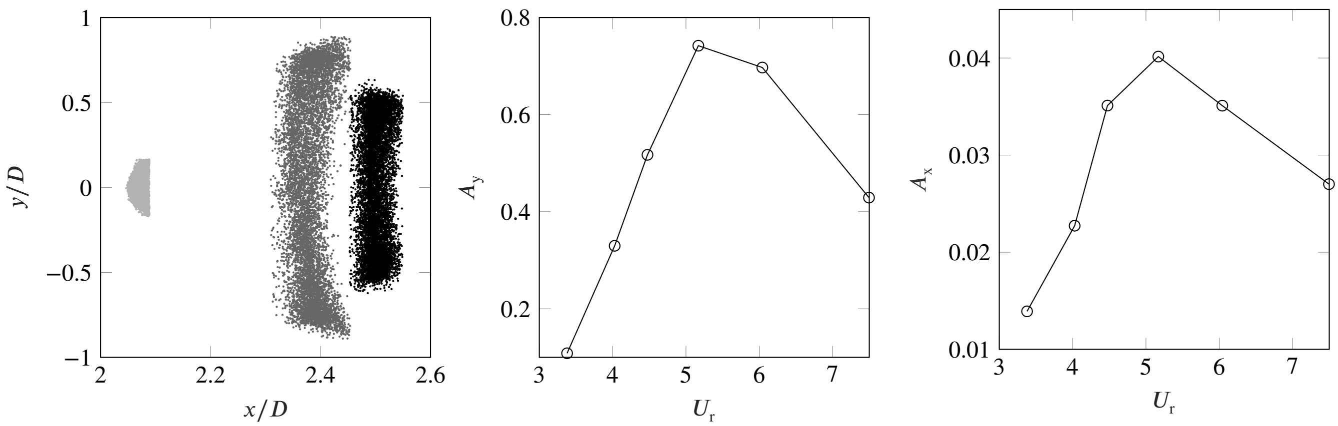

(a) U_r. ●: 3.38. ●: 5.15. ●: 7.5 (b) (c)

Figure 2: Cylinder free end response at $4.5 \times 10^2 \leqslant \mathrm{R_e} \leqslant 1 \times 10^3$. a) Spatiotemporal displacement. b) Maximum displacement in the crossflow direction. c) Maximum displacement in the streamwise direction.

tween a Pixel and real-world coordinates. The wake zone and cylinder response were measured at six flow rates at 70 Hz for two minutes. The PIV measurement consisted of a vertical plane through the cylinder centreline and four horizontal planes at $(x, y, z) = (x, y, [20, 34, 52, 60]D)$. Figure 1 shows a sketch of a vertical (Figure 1a) and horizontal (Figure 1b) measurement. A multiple-pass correlation process with subpixel accuracy of 0.1 pixels were used to determine the flow velocity field from the flow images. An initial interrogation window of 64x64 pixel with two passes, followed by a 32x32 pixel window with three passes were employed. In each correlation, an overlap of 75% between interrogation windows was used to increase the resolution of the velocity field. The maximum spatial resolution was 0.39 mm. The images of the cylinder free end response were calibrated using the same procedure but with a smaller calibration plate LaVision model 058-5. The cylinder response was estimated using the image-based tracking technique described in Mella et al. (2019).

A free decay test was conducted on the bottom-fixed cylinder to determine its damping ratio and the natural frequency measured in air f_{air} and still water f_{water}. The cylinder was subjected to a uni-dimensional displacement parallel and perpendicular to the flow direction. A PS3 Eye Camera was placed on the free end of the cylinder and recorded its response. Each video sequence was taken at 187 Hz with a 320x240 pixel resolution. The images were calibrated using the same procedure described for the cylinder free end response. The results show that the natural frequency measured in air and still water is equal in both directions, with values of $f_{\mathrm{air}} = 6.4$ Hz and $f_{\mathrm{water}} = 5.3$ Hz respectively. Considering a logarithmic decay response, the damping ratio measured in air was estimated at 4%. The free decay test was repeated after all the tests were completed with no degradation on the dynamical properties of the cylinder.

4. Results

4.1. Cylinder response and modal decomposition

Figure 2 summarises the cylinder response over the range of tested U_{r}. Figure 2a shows the spatiotemporal free end displacement at $U_{\mathrm{r}} = [3.38, 5.15, 7.5]$ obtained with the image-based tracking technique described in Mella et al. (2019). The mean streamwise free end position of the cylinder moves downstream as U_{r} increases, reaching a maximum constant displacement of $2.5D$ and an inclination of approximately 1.5° at the maximum flow velocity. Figure 2a suggests that the total cylinder response is composed of a main coherent motion with a superimposed random component. The visualisation of this large-scale pattern will be addressed later by means of the POD technique. Figures 2b and 2c show the maximum displacement in the streamwise A_{x} and crossflow A_{y} direction. Following the definition of Hover et al. (1998), the maximum displacement in a given direction is the mean value of the highest 10% of the recorded response. The maximum displacement in both directions increases with U_{r}, reaching a maximum value of $A_{\mathrm{y}} = 0.74D$ and $A_{\mathrm{x}} = 0.04D$ at $U_{\mathrm{r}} = 5.15$. Then, at further increments of U_{r}, the maximum displacement decreases reaching $A_{\mathrm{y}} = 0.43D$ and $A_{\mathrm{x}} = 0.03D$ at $U_{\mathrm{r}} = 7.5$. The ratio $A_{\mathrm{y}}/A_{\mathrm{x}}$ ranges from 8 at $U_{\mathrm{r}} = 3.18$ to 19 at $U_{\mathrm{r}} = 6.04$, indicating an overall predominance of the crossflow motion over its streamwise counterpart.

Eight minutes of displacement data were separated in vectors of equal length L and arranged in matrix form as described in section 2. Given a fixed measurement time, the selection of L is a trade-off between the number of snapshots used for POD and the cylinder trajectory traced within each snapshot. Convergence of the first (average) and second (variance) order statistics is achieved at $L = 560$ data points. Thus, snapshots of $L = 700$ (53 motion cycles on average) were selected for analysis. The relative modal value ε_i of the first eight modes ($i = [1, ..., 8]$) is shown in Figure 3a. The first two modes capture an important part of the total

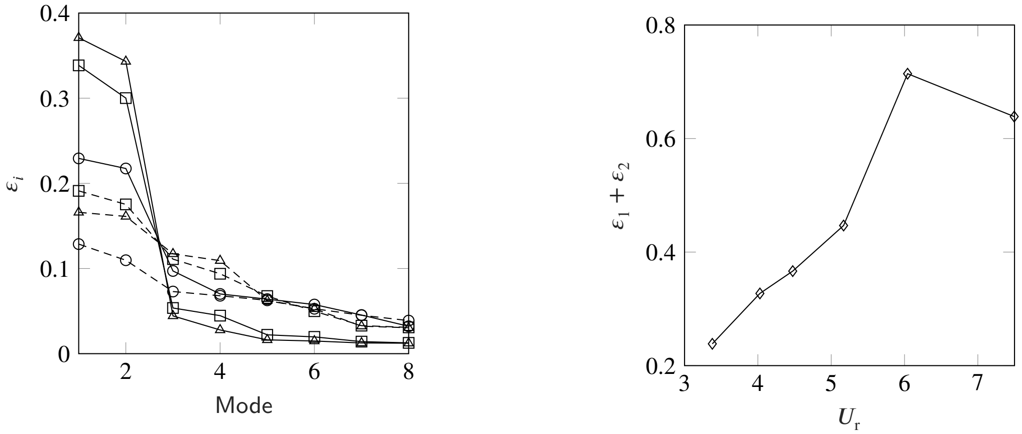

(a) U_{r}. -o-: 3.38, -△-: 4.03, -□-: 4.5, —o—: 5.15, —△—: 6.04, —□—: 7.5

(b)

Figure 3: Relative modal values of the cylinder response. a) ε_i, where $i = [1, 2, ..., 8]$. b) $\varepsilon_1 + \varepsilon_2$

variance at higher cylinder responses ($U_{\mathrm{r}} > 5$) as opposed to lower displacements ($U_{\mathrm{r}} < 5$), from which the relative energy of higher-order modes are significant. It is expected that the first two modes contain relevant trajectory patterns underlying the total displacement for $U_{\mathrm{r}} > 5$ and that the motion history for $U_{\mathrm{r}} < 5$ has no coherent spatial mode. Figure 3b shows the contribution of $\varepsilon_1 + \varepsilon_2$ at different U_{r}. $\varepsilon_1 + \varepsilon_2$ increased up to 45% at the maximum cylinder response. Then, it jumped to 71% when the maximum crossflow displacement decreased from its maximum value of $A_{\mathrm{y}} = 0.74D$ to $A_{\mathrm{y}} = 0.7D$. Lastly, it decreased to 63% when $A_{\mathrm{y}} = 0.43D$ at the highest tested U_{r}. This increment in the predominance of the trajectory pattern to the total body motion after the cylinder reached its maximum response could be explained by a transition to the lower branch, characterised by a higher periodic motion compared to the upper branch (Khalak and Williamson (1999)).

Figure 4 shows the reconstructed displacement signal adding the spatial modes $\mathbf{\Phi}_1 + \mathbf{\Phi}_2$. Higher order modes only contributed to the irregularity of the trajectory patterns for all U_{r}. Irregular modal shapes were obtained for $U_r < 5$. Clockwise elliptical-type trajectories were identified for $U_{\mathrm{r}} = 5.15$ and $U_{\mathrm{r}} = 6.04$. Elliptical trajectories are associated with strong structural coupling between the streamwise and transverse motion (Kheirkhah et al. (2012, 2016)). Similar findings were observed in Oviedo-Tolentino et al. (2014) for a bottom-fixed cylinder with $m^* = 8.13$. Pure elliptical-type trajectories were observed for $U_{\mathrm{r}} > 5$, while irregular shapes were obtained at lower reduced velocities. The researchers suggested that irregular shapes could be associated with a high dependence of the added mass to low U_{r} values. A deviation from a pure elliptical-type trajectory is observed at $U_{\mathrm{r}} = 7.5$. A Power Spectral Density (PSD) analysis of its second spatial mode showed that the energetic value of the first harmonic in the streamwise direction is 83% of its main frequency. The influence of this harmonic explains this particular combination between an elliptical- and eight-type trajectory. Despite the unclear trajectories in Figure 4, the main vibration frequencies of the first two spatial modes were successfully extracted using a PSD analysis. The results are summarised in Table 1. The main frequency in the streamwise f_{x} and crossflow f_{y} direction was normalised by f_{water}. Here, the average of the first mode between f_{x} and f_{y} is defined as the main peak frequency of the cylinder f_{c}. The results show that f_{x} and f_{y} have similar values throughout U_{r}, which is consistent with an elliptical-type trajectory. f_{c} ranges between 0.76 to 1.03 as U_{r} increases. The cylinder achieves its maximum response when $f_{\mathrm{c}} \approx 1$ at $U_{\mathrm{r}} = 5.15$, which is consistent with the findings of Oviedo-Tolentino et al. (2014).

Table 1
Streamwise and crossflow normalised frequencies of the first two modes at different U_{r}

Axis	Mode	U_{r}					
		3.38	4.03	4.5	5.15	6.04	7.5
X	1	0.76	0.86	0.90	1.01	1.02	1.04
	2	0.76	1.68	0.90	1.01	1.02	1.03
Y	1	0.76	0.84	0.89	1.01	1.02	1.03
	2	0.76	0.84	0.89	1.01	1.02	1.03
	f_{c}	0.76	0.85	0.90	1.01	1.02	1.04

4.2. Spanwise synchronisation region

Spanwise wake dynamics were analysed using two-dimensional PIV measurements at a vertical plane through the cylinder centreline and four horizontal planes at $(x, y, z) = (x, y, [20, 34, 52, 60]D)$. The lowest flow measurements ($U_{\mathrm{r}} = 3.38$ and $U_{\mathrm{r}} = 4.03$) are not presented in this section as the results are similar to $U_{\mathrm{r}} = 4.5$. Figure 5 shows the reduced velocity profile at $8D$ upstream from the centre of the cylinder $U_{\mathrm{r}}(x = -8D, y, z)$. Dashed lines indicate the average incoming reduced velocity. The velocity profile resembles a parabolic distribution as expected from

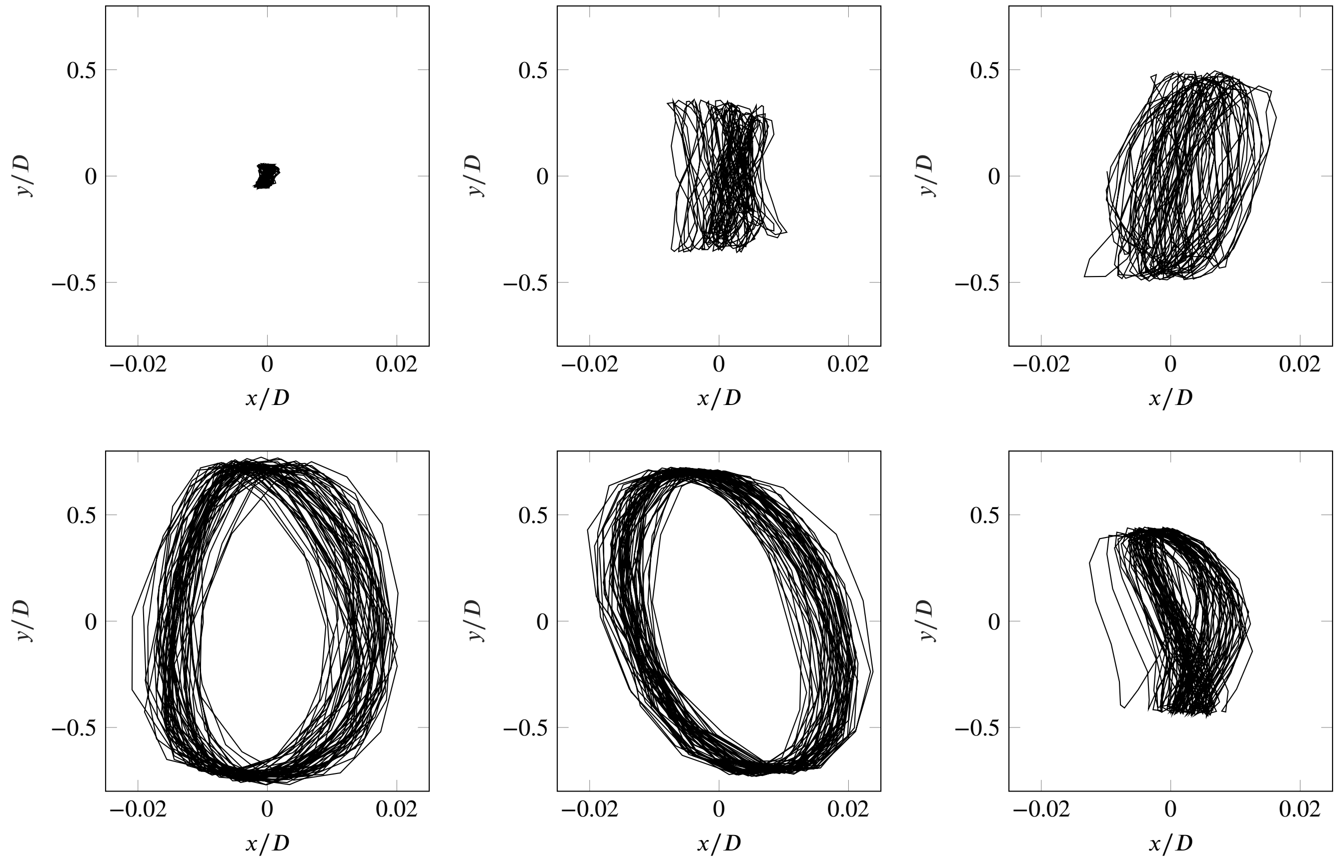

Figure 4: Reconstructed cylinder response from $\mathbf{\Phi}_1 + \mathbf{\Phi}_2$. From top left to bottom right: $U_\mathrm{r} = [3.38, 4.03, 4.5, 5.15, 6.04, 7.5]$.

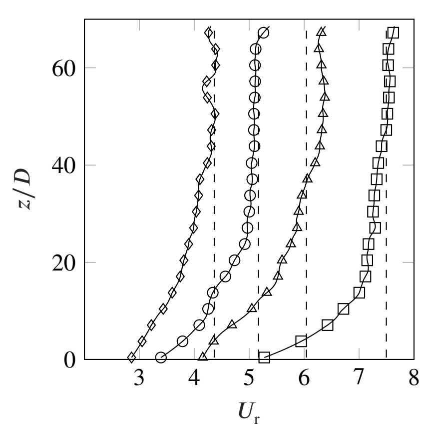

Figure 5: Spanwise reduced velocity profile at $8D$ upstream from the centre of the cylinder. $U_\mathrm{r}(x = -8D, 0, z)$. ◇: 4.5, ○: 5.15, △: 6.04, □: 7.5. Dashed lines are the average incoming reduced velocity calculated using U_inlet

open-channel flows. Approximately 90% of the average incoming reduced velocity is achieved at $z > 18D$. As will be shown later, the velocity gradient at $z < 18D$ had a limited impact on the spanwise synchronisation between the vortex shedding and cylinder main motion frequency.

The spatiotemporal variability of the streamwise velocity component $u(x, y, z, t)$ was analysed to compare its vortex shedding frequency f_v to the main peak frequency of the cylinder f_c. The streamwise velocity is decomposed as $u(x, y, z, t) = u'(x, y, z, t) + \overline{U}(x, y, z)$, where u' is the fluctuating component, and $\overline{U}$ is the time-averaged velocity. The PSD of $u'(4.8D, 0, z, t)$ was calculated at each grid point within z. Figure 7 shows the main peak frequency of the PSD normalised by f_c. Across all reduced velocities, there is a region between $9D$ and $16D$ from the bed surface where $f_\mathrm{v} < f_\mathrm{c}$. This low f_v region is the result of the interaction between a sheared incoming flow velocity, which is produced by the parabolic velocity profile of the open-channel shown in Figure 5, and the presence of the cylinder with a small response amplitude in that region. Analysis of the mean streamwise velocity field downstream of the cylinder showed that $\overline{U}(4.8D, 0, z) \approx U_\mathrm{inlet}/2$ at $z < 16D$ which is in line with the observed reduction in the vortex shedding frequency in that region. Figure 7a and 7b show good agreement between f_v and f_c at $z > 16D$ for $U_\mathrm{r} = 4.5$ and $U_\mathrm{r} = 5.15$ respectively. Specifically, Figure 7b shows that the maximum cylinder response is achieved when the equivalence $f_\mathrm{c} = f_\mathrm{v} = f_\mathrm{water}$ is preserved along the span of the cylinder, i.e. when the spanwise synchronisation region is maximal. It is worth noting that, despite the parabolic distribution of the incoming velocity profile, the synchronisation region extends from $z = 16D$ up to the free surface. The constrained desynchronised region of $z < 16D$ for all

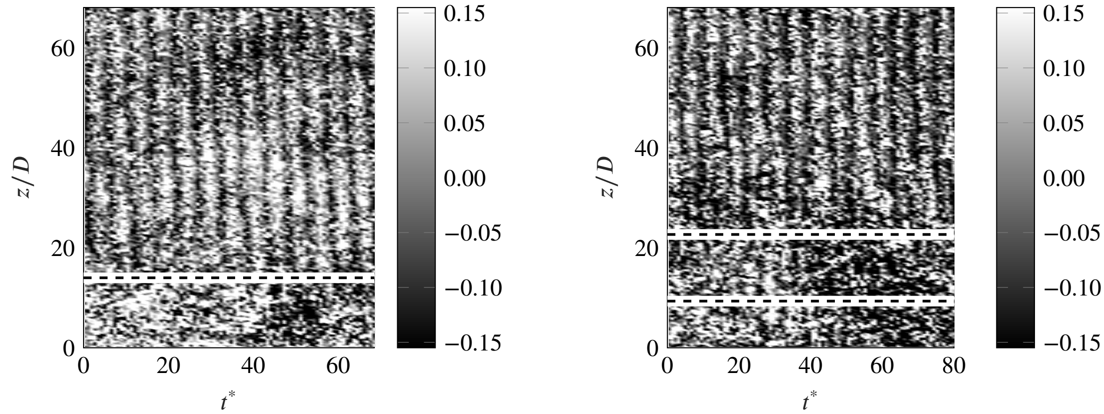

(a) $U_r = 5.15$ (b) $U_r = 6.04$

Figure 6: Normalised time series of $u'(4.8D, 0, z, t)/\overline{U}(4.8D, 0, z)$.

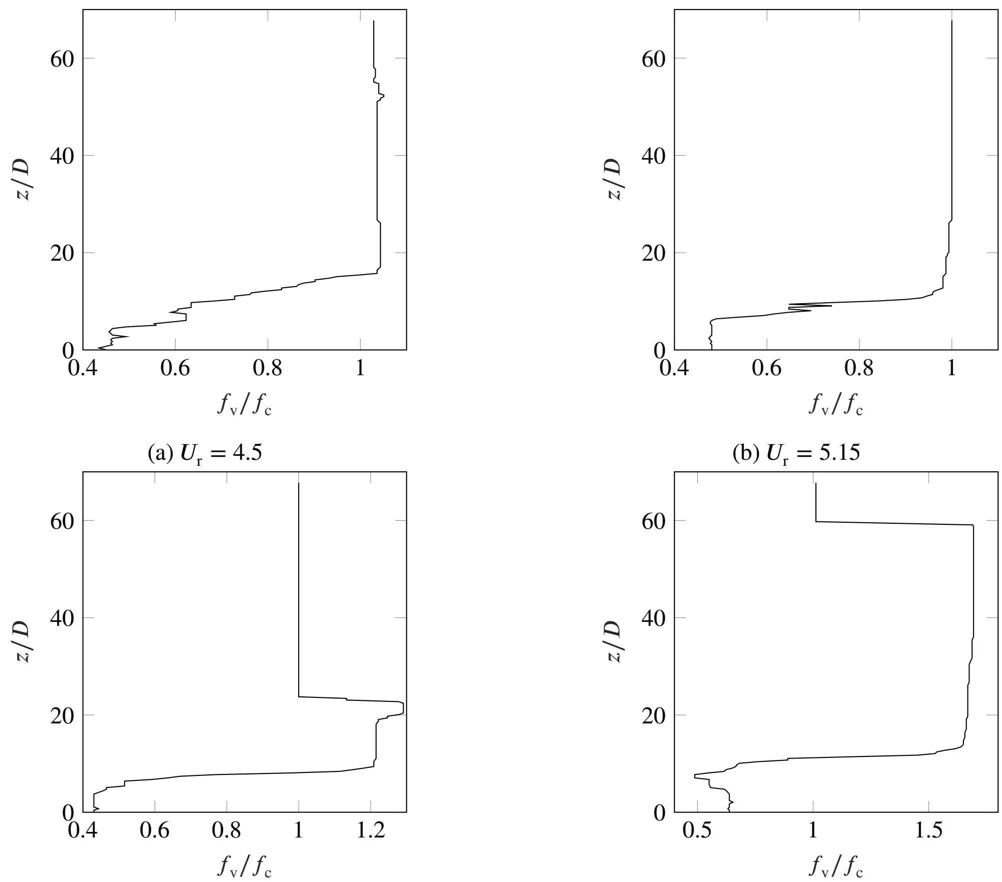

(a) $U_r = 4.5$ (b) $U_r = 5.15$

(c) $U_r = 6.04$ (d) $U_r = 7.5$

Figure 7: Normalised vortex shedding frequency measured at $4.8D$ downstream from the cylinder centre.

U_r is expected to have a small impact on the maximum cylinder response due to its proximity to the cylinder fixed end. At higher U_r, Figure 7c shows an increment of f_v between 1.2 and 1.3 at $9D \leqslant z \leqslant 25D$. Likewise, at the maximum tested U_r, f_v jumped from 1.01 to between 1.65 and 1.70 at $13D \leqslant z \leqslant 59D$. In terms of maximum crossflow displacement, A_y reaches its maximum value of $0.74D$ when the synchronisation region is maximal. Then, A_y decreased 5.4% and 39.7% when the desynchronised region extended $17D$ and $53D$, respectively. Figure 6 shows the time series of $u'(4.8D, 0, z, t)$, normalised by $\overline{U}(4.8D, 0, z)$, for $U_r = 5.15$ and $U_r = 6.04$. Here, the normalised time was defined as $t^* = tU_{\text{inlet}}/D$. Wake patterns are clearly visible for both Ur. The extension of these wake patterns, delimited by hori-

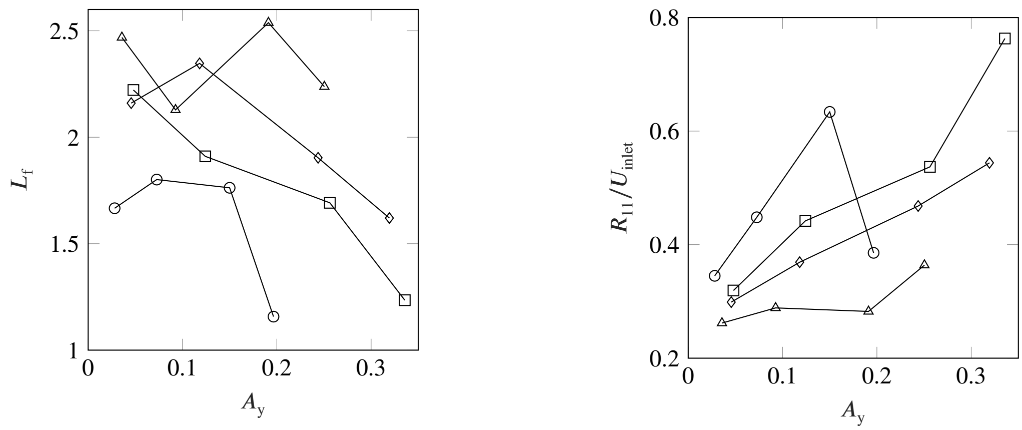

(a) U_r. –○–: 4.5, –□–: 5.15, –◇–: 6.04, –△–: 7.5.

(b) U_r. –○–: 4.5, –□–: 5.15, –◇–: 6.04, –△–: 7.5.

Figure 8: L_f and maximum R_{11} at different water depths.

zontal lines, coincided with the regions where $f_v = f_c$. The additional horizontal line in Figure 6b delimits an intermediate region where $f_v > f_c$. Overall, Figure 6 and 7 show the development of a bottom-up desynchronisation process, starting at $z = 16D$ and moving towards the free surface as U_r increases.

Wake dynamics as the desynchronisation process develops are analysed in terms of fluctuating velocity fields. Figure 8 shows the vortex formation length L_f and the maximum normal Reynold Stress $R_{11} = \overline{u'u'}/U^2_{inlet}$ along the wake centreline at $(x, y, z = [20, 34, 52, 60]D)$. The formation length corresponds to the downstream distance from the cylinder surface where the maximum R_{11} is achieved. L_f and the maximum R_{11} are plotted against its corresponding local maximum crossflow cylinder displacement $A_y(z)$, which was estimated assuming a linear-elastic response. A general reduction of L_f is observed as $A_y(z)$ increases in the synchronised region (see $U_r = [4.5, 5.15]$ in Figure 8a). In contrast, the maximum R_{11} increases with $A_y(z)$. These results are in line with Bearman (1984), which indicated that higher cylinder displacements lead to stronger and shorter vortex formation near the cylinder with a subsequent stronger vortex shedding. At $U_r = 6.04$, L_f increases from $2.16D$ to $2.35D$ as the plane of measurement moves from a desynchronised region ($z = 18D$) to a synchronised one ($z = 34D$). Then, L_f restores it inverse relationship with $A_y(z)$ for $z > 34D$ in the synchronised region. At $U_r = 7.5$, where only $z \geq 59D$ is synchronised, L_f ranges between $2.2D$ and $2.5D$ and no clear trend is observed. In contrast, the maximum R_{11} slowly increases from 0.26 to 0.28 throughout its desynchronised region ($z < 59D$) and then jumps to 0.36 at $z = 60D$, where the cylinder and wake are still synchronised. A significant reduction in L_f and maximum R_{11} is observed at $z = 60D$ for $U_r = 4.5$. The R_{11} distribution along the wake centreline shows a double peak in its vortex formation region which suggest the confluence between two vortex pattern configurations. Nevertheless, further research needs to be conducted to analyse this particular case.

The desynchronisation process described above can be partially explained by the particular characteristics of the tested bottom-fixed cylinder. Flemming and Williamson (2005) showed that, for small streamwise amplitudes, cylinders with two- and one-DOF free-vibration agree qualitatively well. Furthermore, Williamson and Roshko (1988) indicated that the synchronisation range, dependent on the timing between the cylinder-fluid acceleration, increases with the cylinder displacement. The bottom-fixed cylinder has a dominant crossflow response up to 19 times its streamwise counterpart. Consequently, the range of crossflow response acceleration along the span of the cylinder, which diminishes to zero approaching its fixed end, is largely responsible for the range of U_r in which synchronisation occurs. As U_r increases and the cylinder motion is significant, the synchronisation region along the span of the cylinder is maximal, and the vortex shedding frequency is locked-in to the cylinder motion frequency. This relationship is preserved at higher U_r until $f_c = f_{water}$, where the maximum cylinder displacement is achieved. Then, at further increments of U_r, the cylinder displacement near its fixed end is not able to reach the needed increment in acceleration to sustain a synchronised condition, and desynchronisation occurs. As a consequence, the vortex region strength along the span of the cylinder decreases with a subsequent reduction in the cylinder response. This desynchronisation process is enhanced as the desynchronised region develops towards the water surface, with a higher percentage of the cylinder response along its span being unable to sustain lock-in, reducing the overall strength of the vortices, and causing a systematic reduction in the cylinder response. Further changes are observed in the vortex pattern as the desynchronisation region progresses. Figure 9 shows the contours of normal Reynold stress $R_{11} = \overline{u'u'}/U^2_{inlet}$ at $z = [34, 52, 60]D$. Important changes are observed as z increases, specifically at $z = 60D$. Following the contour distribution in Govardhan and Williamson (2001), a transition from 2S vortex mode (Figure 9a) to 2P (Figures 9b and 9c) is observed. Then, Figure 9d suggest a transition back to a 2S vortex pattern

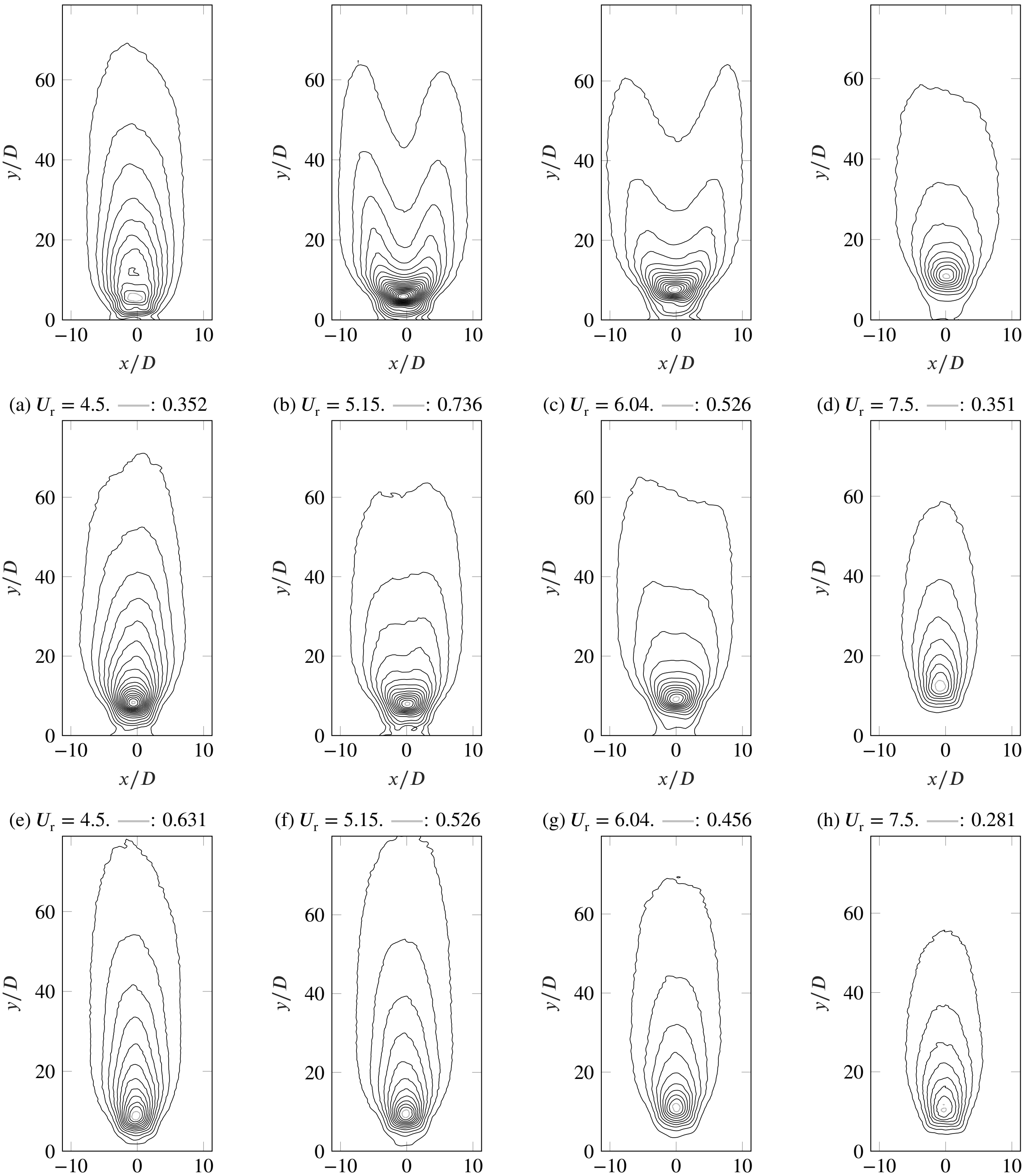

(a) $U_\mathrm{r} = 4.5$. —: 0.352 (b) $U_\mathrm{r} = 5.15$. —: 0.736 (c) $U_\mathrm{r} = 6.04$. —: 0.526 (d) $U_\mathrm{r} = 7.5$. —: 0.351

(e) $U_\mathrm{r} = 4.5$. —: 0.631 (f) $U_\mathrm{r} = 5.15$. —: 0.526 (g) $U_\mathrm{r} = 6.04$. —: 0.456 (h) $U_\mathrm{r} = 7.5$. —: 0.281

(i) $U_\mathrm{r} = 4.5$. —: 0.424 (j) $U_\mathrm{r} = 5.15$. —: 0.421 (k) $U_\mathrm{r} = 6.04$. —: 0.351 (l) $U_\mathrm{r} = 7.5$. —: 0.282

Figure 9: Contours of $\overline{u'u'}/U_\mathrm{inlet}^2$ (contour interval = 0.035) at $z = 60D$ (a-d), $z = 52D$ (e-h) and $z = 34D$ (i-l). Grey line: maximum contour value.

at the highest U_r. A 2S-2P dual-mode configuration is observed across the span of the cylinder for $U_\mathrm{r} = 5.15$ (Figures 9b, 9f, and 9j) and $U_\mathrm{r} = 6.04$ (Figures 9c, 9g, and 9k).

5. Conclusions

This study analyses the spanwise vortex shedding dynamics and structural response of a bottom-fixed cylinder subjected to a range of open-channel, fully developed turbulent flows. Planar PIV measurements and a synchronised single camera were used to capture the flow around the wake region and the cylinder free end response. The results showed that the POD technique successfully uncovers the main trajectory patterns in cases where the cylinder response is highly modulated. The patterns uncovered for the tested cylinder correspond to a clockwise elliptical-type trajectory for $U_r > 5$. A deviation from a pure elliptical-type trajectory was found at $U_r = 7.5$, which is given by the relation between the main streamwise frequency of its second spatial mode and its first harmonic. Wake dynamic analysis showed that the maximum response is achieved when the cylinder motion and vortex shedding frequencies are equal (i.e. synchronised) to the natural frequency of the structure measured in still water, and when this equivalence is preserved along the span of the cylinder. As U_r increases, the cylinder displacement near its fixed end is not able to reach the needed increment in acceleration to sustain a synchronised condition, and desynchronisation occurs. As a consequence, the vortex strength is reduced across the span of the cylinder with a subsequent decrement in the cylinder response. As U_r is further increased, the desynchronised region progresses towards the water surface alongside further decrements in vortex strength and a systematic reduction in the cylinder response. Changes in the wake dynamics as the desynchronised region progresses and the cylinder response decreases showed a transition from a 2S-2P dual-mode configuration at the highest cylinder response to a predominant 2S mode. The results showed that, despite the highly three-dimensional experimental conditions under significant turbulent incoming flows, the findings of previous studies based on simpler experimental models can still be used to broadly explain the observed bottom-up desynchronisation process.

Acknowledgement

Work supported by a Doctoral Scholarship from CONICYT/ Concurso para Beca de Doctorado en el Extranjero.

References

Bearman, P., 1984. Vortex Shedding from Oscillating Bluff Bodies. Annual Review of Fluid Mechanics 16, 195–222. doi:10.1146/annurev.fl.16.010184.001211.

Berkooz, G., Holmes, P., Lumley, J., 1993. The Proper Orthogonal Decomposition in the Analysis of Turbulent Flows. Annual Review of Fluid Mechanics 25, 539–575. doi:10.1146/annurev.fl.25.010193.002543.

Brevis, W., García-Villalba, M., 2011. Shallow-flow visualization analysis by proper orthogonal decomposition. Journal of Hydraulic Research 49, 586–594. doi:10.1080/00221686.2011.585012.

Chatterjee, A., 2000. An introduction to the proper orthogonal decomposition. Current Science 78, 808–817.

Flemming, F., Williamson, C.H., 2005. Vortex-induced vibrations of a pivoted cylinder. Journal of Fluid Mechanics 522, 215–252. doi:10.1017/S0022112004001831.

Franzini, G.R., Pesce, C.P., Gonçalves, R.T., Fujarra, A.L.C., Pereira, A.A.P., 2014. Concomitant vortex-induced vibration experiments: A cantilevered flexible cylinder and a rigid cylinder mounted on a leaf-spring apparatus. Journal of the Brazilian Society of Mechanical Sciences and Engineering 36, 547–558. doi:10.1007/s40430-013-0095-x.

Gabbai, R.D., Benaroya, H., 2005. An overview of modeling and experiments of vortex-induced vibration of circular cylinders. Journal of Sound and Vibration 282, 575–616. doi:10.1016/j.jsv.2004.04.017.

Govardhan, R., Williamson, C.H., 2000. Modes of vortex formation and frequency response of a freely vibrating cylinder. Journal of Fluid Mechanics 420, 85–130. doi:10.1017/S0022112000001233.

Govardhan, R., Williamson, C.H., 2001. Mean and fluctuating velocity fields in the wake of a freely-vibrating cylinder. Journal of Fluids and Structures 15, 489–501. doi:10.1006/jfls.2000.0350.

Higham, J.E., Brevis, W., 2018. Modification of the modal characteristics of a square cylinder wake obstructed by a multi-scale array of obstacles. Experimental Thermal and Fluid Science 90, 212–219. doi:10.1016/j.expthermflusci.2017.09.019.

Hover, F.S., Techet, A.H., Triantafyllou, M.S., 1998. Forces on oscillating uniform and tapered cylinders in crossflow. Journal of Fluid Mechanics 363, 97–114. doi:10.1017/S0022112098001074.

Jauvtis, N., Williamson, C.H., 2004. The effect of two degrees of freedom on vortex-induced vibration at low mass and damping. Journal of Fluid Mechanics 509, 23–62. doi:10.1017/S0022112004008778.

Kang, Z., Jia, L., 2013. An experiment study of a cylinder's two degree of freedom VIV trajectories. Ocean Engineering 70, 129–140. doi:10.1016/j.oceaneng.2013.05.033.

Khalak, A., Williamson, C.H., 1996. Dynamics of a hydroelastic cylinder with very low mass and damping. Journal of Fluids and Structures 10, 455–472. doi:10.1006/jfls.1996.0031.

Khalak, A., Williamson, C.H., 1997. Investigation of relative effects of mass and damping in vortex-induced vibration of a circular cylinder. Journal of Wind Engineering and Industrial Aerodynamics 69, 341–350. doi:10.1016/S0167-6105(97)00167-0.

Khalak, A., Williamson, C.H., 1999. Motions, forces and mode transitions in vortex-induced vibrations at low mass-damping. Journal of Fluids and Structures 13, 813–851. doi:10.1006/jfls.1999.0236.

Kheirkhah, S., Yarusevych, S., Narasimhan, S., 2012. Orbiting response in vortex-induced vibrations of a two-degree-of-freedom pivoted circular cylinder. Journal of Fluids and Structures 28, 343–358. doi:10.1016/j.jfluidstructs.2011.08.014.

Kheirkhah, S., Yarusevych, S., Narasimhan, S., 2016. Wake Topology of a Cylinder Undergoing Vortex-Induced Vibrations With Elliptic Trajectories. Journal of Fluids Engineering 138, 054501. doi:10.1115/1.4031971.

Labbé, D.F., Wilson, P.A., 2007. A numerical investigation of the effects of the spanwise length on the 3-D wake of a circular cylinder. Journal of Fluids and Structures 23, 1168–1188. doi:10.1016/j.jfluidstructs.2007.05.005.

Mella, D.A., Brevis, W., Jonathan, H., Racic, V., Susmel, L., 2019. Image-based tracking technique assessment and application to a fluid-structure interaction experiment. Proceedings of the Institution of Mechanical Engineers, Part C: Journal of Mechanical Engineering 233, 5724–5734. doi:10.1177/0954406219853852.

Morse, T.L., Williamson, C.H., 2009. Fluid forcing, wake modes, and transitions for a cylinder undergoing controlled oscillations. Journal of Fluids and Structures 25, 697–712. doi:10.1016/j.jfluidstructs.2008.12.003.

Oviedo-Tolentino, F., Pérez-Gutiérrez, F.G., Romero-Méndez, R., Hernández-Guerrero, A., 2014. Vortex-induced vibration of a bottom fixed flexible circular beam. Ocean Engineering 88, 463–471. doi:10.1016/j.oceaneng.2014.07.012.

Raghavan, K., Bernitsas, M.M., 2011. Experimental investigation of Reynolds number effect on vortex induced vibration of rigid circular cylinder on elastic supports. Ocean Engineering 38, 719–731. doi:10.1016/j.oceaneng.2010.09.003.

Sarpkaya, T., 2004. A critical review of the intrinsic nature of vortex-induced vibrations. Journal of Fluids and Structures 19, 389–447. doi:10.1016/j.jfluidstructs.2004.02.005.

Sirovich, L., 1987. Turbulence and the dynamics of coherent structures. I. Coherent structures. Quarterly of Applied Mathematics doi:10.1090/qam/910462.

Techet, A.H., Hover, F.S., Triantafyllou, M.S., 1998. Vortical patterns behind a tapered cylinder oscillating transversely to a uniform flow. Journal of Fluid Mechanics 363, 76–96. doi:10.1017/S0022112098001104.

Voorhees, A., Dong, P., Atsavapranee, P., Benaroya, H., Wei, T., 2008. Beating of a circular cylinder mounted as an inverted pendulum. Journal of Fluid Mechanics 610, 217–247. doi:10.1017/S0022112008002383.

Wanderley, J.B., Soares, L.F.N., 2015. Vortex-induced vibration on a two-dimensional circular cylinder with low Reynolds number and low mass-damping parameter. Ocean Engineering 97, 156–164. doi:10.1016/j.oceaneng.2015.01.012.

Williamson, C., Govardhan, R., 2004. Vortex-induced vibrations. Annual Review of Fluid Mechanics 36, 413–455. doi:10.1146/annurev.fluid.36.050802.122128.

Williamson, C.H., Roshko, A., 1988. Vortex formation in the wake of an oscillating cylinder. Journal of Fluids and Structures 2, 355–381. doi:10.1016/S0889-9746(88)90058-8.